

THREE-DIMENSIONAL TEMPLATE CORRELATIONS FOR DIRECT-DETECTION LASER-RADAR TARGET RECOGNITION

Douglas G. Youmans, George A. Hart
Schafer Corporation
321 Billerica Rd., Chelmsford, MA 01890

ABSTRACT

Direct-detection laser radars can measure the range and the intensity returns from a target, with or without clutter, for each part of the target resolved in angle by the optical system. Because the ladar's angular resolution is in micro-radians, there are generally at least a few angular pixels "on target." In addition, for narrow pulse ladar systems, there may be ten or so sequential intensity measurements in range per pixel as the laser pulse propagates down the target's surface. The output image is, therefore, potentially a three dimensional "cube" of intensity measurements and quantized in the range axis by the range-bin size or "voxel." This is known as "range resolved angle-angle-intensity" ladar, and one such system is being built by BMDO under the DITP effort.

Transforming this 3D-matrix image into the spatial-frequency domain using 3D-Fourier transforms, we have followed conventional 2D template-correlation techniques to perform target recognition and identification. Results of target image correlations using the "joint transform correlator," "the inverse filter," the "symmetric phase-only matched-filter," and the classical "matched filter" among others are presented. Also, projection of the 3D-matrix image onto the x-y, x-z, and y-z planes allows the use of conventional (2D) correlators, but their outputs must be combined. Simulated far-field test data using conical shaped targets are presented to study the 3D correlators, and the effects of laser speckle are discussed. Recent developments in negative-binomial driven shot-noise effects in range-resolved direct-detection ladar are outlined as well. We note that 3D template correlation may supplement or refine less computationally intensive algorithms such as total signal, range-extent, x-z, y-z, and x-y plane image centroid estimation, and image moments.

1.0 INTRODUCTION

There are many two dimensional image processing algorithms useful in automatic target recognition and identification that can be found in the literature. We summarize some of these in Section 3.0 as developed by the passive sensor community, but now we extrapolate them to three dimensions: elevation, azimuth, range, and intensity per voxel. Even with a single range measurement per elevation / azimuth pixel (current tactical ladars), the effects of laser speckle must be accurately modeled. Recent work has allowed the numerical evaluation of the speckle "M" parameter for arbitrary source region, illumination irradiance, and receiver aperture. These speckle effects are briefly summarized in Section 2.0. In addition, as the photons are detected by a photon-counting photo-multiplier tube, the detector's response and the electronic's bandwidth result in a classical "shot-noise" impulse-response summation process. This is also reviewed in Section 2.0 based on state of the art photomultiplier tube detector data.

Form SF298 Citation Data

Report Date <i>("DD MON YYYY")</i> 00001999	Report Type N/A	Dates Covered (from... to) <i>("DD MON YYYY")</i>
Title and Subtitle Three-Dimensional Template Correlations for Direct-Detection Laser-Radar Target Recognition		Contract or Grant Number
		Program Element Number
Authors		Project Number
		Task Number
		Work Unit Number
Performing Organization Name(s) and Address(es) Schafer Corporation 321 Billerica Rd. Chelmsford, MA 01890		Performing Organization Number(s)
Sponsoring/Monitoring Agency Name(s) and Address(es)		Monitoring Agency Acronym
		Monitoring Agency Report Number(s)
Distribution/Availability Statement Approved for public release, distribution unlimited		
Supplementary Notes		
Abstract		
Subject Terms		
Document Classification unclassified		Classification of SF298 unclassified
Classification of Abstract unclassified		Limitation of Abstract unlimited
Number of Pages 16		

The 3D template correlation results to date are described in Section 5.0. Simple diffuse cone, sphere, and cylinder numerical targets without clutter are used in this initial work and are described in Section 4.0.

2.0 SUMMARY OF LADAR SPECKLE AND SHOT-NOISE EFFECTS

In order to accurately simulate ladar target images for algorithm development, it is necessary to have the correct laser radar speckle and detector response models. In this section we review laser speckle theory, photon counting statistics, and the detector with electronics bandwidth and resulting shot-noise stochastic process effects. Round-trip turbulence modulation of the Poisson counting statistics are also mentioned, but no further analysis of endo-atmospheric ladar will be presented in this paper.

2.1 SPECKLE IRRADIANCE STATISTICS

When laser light is back-scattered from a rough target, constructive and destructive interference results in the well known "laser speckle" pattern distribution back at the receiving aperture. Goodman¹⁻⁴ has shown that the sum of a number of uncorrelated irradiances, collected by the finite size ladar receiving aperture, has a probability density function given by:

$$p_{\Sigma}(I) = \sum_{k=1}^M \langle I_k \rangle^{M-2} \exp(-I/\langle I_k \rangle) \prod_{\substack{p=1 \\ p \neq k}}^M (\langle I_k \rangle - \langle I_p \rangle) \quad (1)$$

This can be approximated by a simpler gamma distribution given by

$$p_{\Sigma}(I) \cong \frac{(M/\langle I \rangle)^M I^{M-1} \exp(-MI/\langle I \rangle)}{\Gamma(M)} \quad (M \geq 1) \quad (2)$$

The "M" parameter was shown by Goodman³ to be equal to the reciprocal normalized-variance-of-irradiance

$$\frac{1}{M} \equiv \frac{\sigma_{I_{rec}}^2}{\langle I \rangle^2} = \frac{1}{A_{rec}^2} \iint R_{Arec}(\Delta x, \Delta y) |\mu_E(\Delta x, \Delta y, z)|^2 d\Delta x d\Delta y \quad (3)$$

where R_{Arec} is the "autocorrelation function" of the ladar receiving aperture, and μ_E is the "complex coherence factor" or "spatial coherence function"⁴ given by the inverse Fourier transform of the irradiance from the target source region (ξ, η) being measured:

$$\mu_E(\Delta x, \Delta y, z) \equiv \frac{\iint |E(\xi, \eta)|^2 \exp\left(\frac{j2\pi}{\lambda z} (\xi \Delta x + \eta \Delta y)\right) d\xi d\eta}{\iint |E(\xi, \eta)|^2 d\xi d\eta} \quad (4)$$

where $\Delta x = (x_1 - x_2)$ and $\Delta y = (y_1 - y_2)$ over the receiving aperture. The back-propagated pixel sensitive region must be at least $2.44 \lambda / D \times 2.44 \lambda / D$ in angular dimension, due to diffraction by the receiving aperture. The numerical evaluation of "M" for arbitrary source region irradiance (an illuminated single pixel range-bin on target) and arbitrary aperture geometry versus range z was described in a recent paper⁵.

2.2 PHOTON COUNTING STATISTICS

When counting individual photons, as when using photo-multiplier tubes, an "inhomogeneous" or "doubly stochastic" Poisson process^{3,4} results where the Poisson counting probability density function (pdf) is averaged over the statistics of the fluctuating received energy:

$$p_S(n) = \int_0^\infty \left[\frac{(\alpha E)^k}{k!} \exp(-\alpha E) \delta(n-k) \right] p_E(E) dE \quad (5)$$

Here, α is $\eta/h\nu$, the detector quantum efficiency divided by the photon energy, and n may equal 0, 1, 2, 3, etc. discrete events. The energy, E , is the received irradiance, I , multiplied by the receiver area and the integration or counting time, T . Averaging the photo-electron counts over the gamma distribution of equation (2), corresponding to M independent correlation cells with identical average intensities, the discrete "negative-binomial" distribution^{1,2,4} results:

$$p_S(n) = \sum_{k=0}^{\infty} \frac{\Gamma(k+M)}{k! \Gamma(M)} \left(1 + \frac{M}{N_S}\right)^{-k} \left(1 + \frac{N_S}{M}\right)^{-M} \delta(n-k) = \sum_{k=0}^{\infty} P_S(k) \delta(n-k) \quad (6)$$

The lower case letters indicate a "pdf," whereas the upper case letters represent the discrete probabilities of the pdf. The mean of " n " is denoted as N_S , where " S " denotes signal, as opposed to dark-counts (D) or background-counts (B). The variance of n is $\sigma_n^2 = N_S + N_S^2/M$. The pdf $p_S(n)$ becomes Poisson for $M \gg N_S$ and Bose-Einstein distributed for $M \ll N_S$.

We also point out that when converting the photon statistics to photo-electron statistics, a new negative-binomial distribution results⁶ having a mean count number which is reduced by the quantum efficiency of the photo-cathode surface or semiconductor absorption region ($\eta \times N_S$). The M parameter remains the same, however.

When a target voxel has a glint component, a constant intensity in time is observed, by definition of a glint. This is like looking at a very weak corner-cube-retroreflector. In equation (5) $p(E)$ would become a delta function, and the counting statistics are Poisson. If we assume the glint component is independent of the diffuse component, hence, no interference, then the photon counts are the sum of the two processes and the pdf is the convolution of a negative-binomial and a Poisson. These pdf's have been evaluated in the literature and will not be discussed here.

2.3 DETECTOR AND ELECTRONICS SHOT-NOISE EFFECTS

In reality, the photons returning from a target are spread over time as are the electron pulses produced by a PMT. These distributed electron pulses are amplified and filtered by the electronics prior to digitization and signal processing. The voltage pulse per photo-electron event pulse is known as the "impulse-response-function" of the electronics, $h(t)$. The impulse response is usually an exponential decay or triangular shape depending on the filter bandwidths and frequency roll-offs. The shot noise random process^{10,11} is defined as the sum of these voltage impulse responses :

$$v(t) = \sum_i h(t - t_i) \quad (7)$$

where $h(t)$ is the impulse response of the detector and the electronics, and the t_i are random points in time due to the negative-binomial process described in (6) and its Poisson or Bose-Einstein limits. For a fixed counting time, the number of t_i photo-electron events is " n " with pdf $p_S(n)$.

The probability density function of $v(t)$ is constructed following Papoulis¹⁰ as

$$p_V(v) = \sum_{n=0}^{\infty} P_S(n) g_n(v) \quad (8)$$

where $g_0(v)$ is defined to be a delta function, $g_1(v)$ is the voltage pdf of the impulse response function $h(t)$ (ordinarily denoted $p_h(v)$) and, for $n \geq 2$, $g_n(v)$ is the n^{th} -convolution of $g_1(v)$, i.e., $g_1 \otimes g_1 \otimes g_1 \dots \otimes g_1$ $n-1$ times. The " g_n " are the "conditional densities" of v , conditioned on the result that $n = 0, 1, 2, 3$ etc. photo-electron events has occurred at a given time. The probability density function of $h(t)$, denoted by $g_1(v)$,

can be geometrically determined from $h(t)$ which is in volts vs time. For a **triangular** impulse response function we find

$$g_1(v) = \begin{cases} \frac{1}{v_{\max} - v_{\min}} & \text{for } v_{\min} \leq v \leq v_{\max} \\ 0 & \text{otherwise} \end{cases} \quad (9)$$

which is a uniform pdf centered at $(v_{\max} + v_{\min})/2$.

Photo-multiplier tube detectors have a small variation in the peak of their single photo-electron event output electron pulses, exclusive of the baseline noise, known as the “pulse height distribution.” We may model this by assuming that the impulse responses are triangles with varying height. The voltage probability density function is then given by equation (9) with varying v_{\max} . We make v_{\max} a Gaussian (Normal) random number with mean equal to “PV” peak volts and a variance equal to $c_1 \times PV$:

$$g'_1(v) = \begin{cases} \frac{1}{(PV + N(0, c_1 PV)) - v_{\min}} & \text{for } v_{\min} \leq v \leq v_{\max} \\ 0 & \text{otherwise} \end{cases} \quad (10)$$

“PV” is the mean peak voltage of 2.3 mV peak per photo-electron, and $c_1 = 5 \times 10^{-5}$ for a high performance Intevac²² photo-multiplier tube. Many Monte Carlo runs are made, and the average of the runs is used as g'_1 . The minimum voltage is zero since $h(t)$ is nonnegative. The set of g'_n conditional densities are then computed by multiple convolutions as above.

Since we also have additive Gaussian baseline noise, we must also convolve the g'_n conditional densities with a normal distribution with zero mean and baseline-noise standard deviation σ_n . Equation (8) for the lidar detector output then becomes

$$p_V(v) = \sum_{n=0}^{\infty} P_S(n) [g'_n(v) \otimes N(0, \sigma_n^2)] \quad (11)$$

per pixel range-bin.

Figures 1A and 1B show data²² for a 1 m diameter, 2 m long cone at a simulated 141 km distance. An Intevac intensified vacuum photo-diode with avalanche-diode gain detector was used. The dashed line in Figure 1B is an analytical gamma pdf (based on equation (2)) that may be used to generate continuous random voltage samples for a pixel range-bin output given N_S and M for that voxel. Scaling the gamma pdf of equation (2) by $N_S^{0.83}$ and $M^{0.7}$ using $N_V \equiv N_S^{0.83}$ and $M_V \equiv M^{0.7}$:

$$p_V(v) \cong \frac{(M_V / (N_V \times PV))^{M_V} v^{M_V-1} \exp(M_V v / (N_V \times PV))}{\Gamma(M_V)} \quad (12)$$

gives a good fit²² to the shot-noise voltage pdf for one or more photo-electron events. Zero photo-electron events (sampling of the baseline noise) will, of course, be thresholded out. Equation (12) reflects the degradation of the gamma irradiance distribution by the Poisson photon-detection process -- a reduced effective mean and a smaller effective M . This distribution can be used for quickly generating speckled target realizations during Monte Carlo runs for algorithm development. It is effectively a smoothed negative-binomial driven shot-noise pdf based on the Intevac PMT characteristics.

2.4 ROUND-TRIP TURBULENCE EFFECTS (ENDO-ATMOSPHERIC SCENARIOS)

Round-trip passage lidar scintillation from **resolved** targets has been well characterized in the literature by Holmes and Gudimetla¹²⁻¹⁵. They found that a "two-parameter K distribution" irradiance distribution fits the data and theory of round-trip propagation effects well:

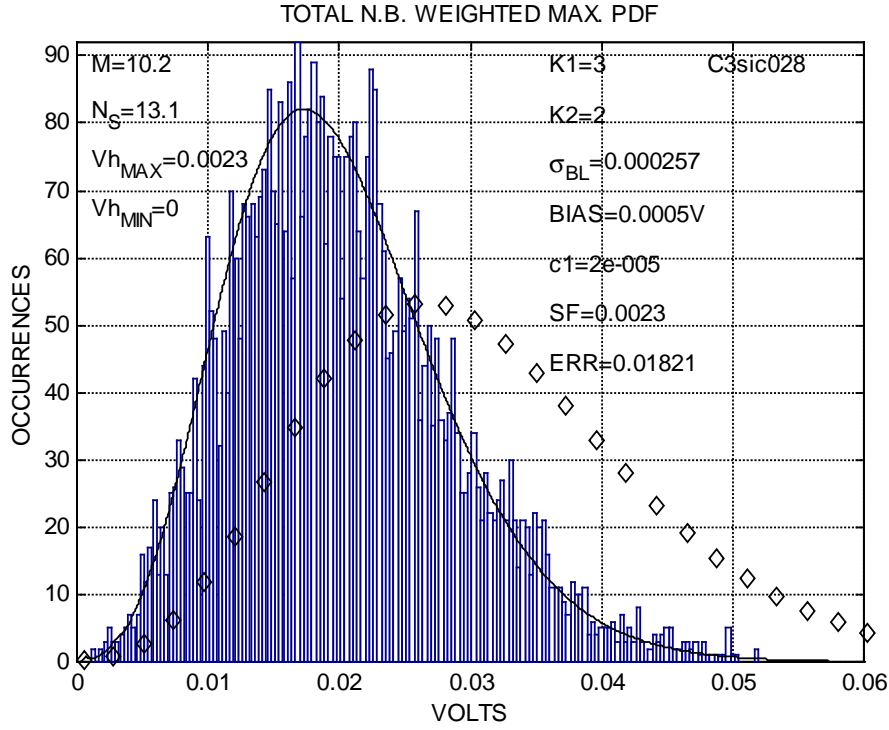


Figure 1A. Histogram data fit²² (solid line) to range-bin #6 of a 2 m long cone at 141 km.

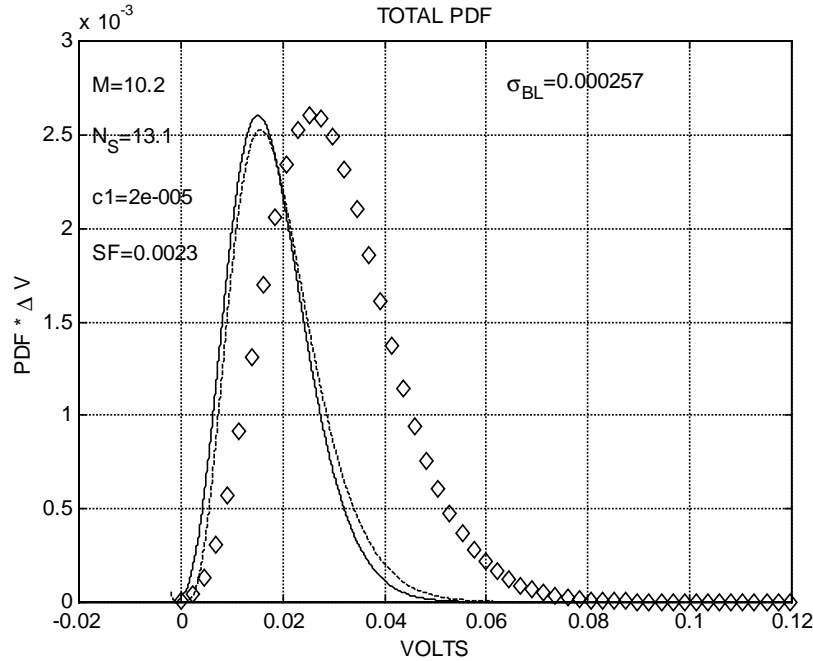


Figure 1B. Probability density function determined by least-squares error data fit using equation (11), solid line. Dashed line is simple pdf fit given by equation (12) for fast Monte Carlo realizations. Diamonds are negative-binomial discrete event probabilities in the absence of random impulse-response summation (shot-noise)²².

$$p_{I_n}(I_n) = \frac{(M_l M_t)^{(M_l+M_t)/2}}{\Gamma(M_l) \Gamma(M_t)} 2 I_n^{(M_l+M_t)/2-1} K_{|M_l-M_t|} \left(2 (M_l M_t I_n)^{1/2} \right) \quad (13)$$

where K is the modified Bessel function of the second kind, I_n is the normalized intensity ($I / \langle I \rangle$), and M_l is the number of uncorrelated laser modes and M_t is the "turbulence M parameter." These are related to the normalized-intensity-variance by

$$\sigma_{I_n}^2 = \left(1 + \frac{1}{M_l} \right) \left(1 + \frac{1}{M_t} \right) - 1 \quad (14)$$

The aperture-averaged normalized-intensity-variance due to turbulence is approximated by

$$\sigma_{I_n}^2 = \exp(\gamma 4 \sigma_{\mathcal{H}}^2) - 1 \quad (18)$$

which is reduced by aperture averaging via the factor γ , the "aperture-averaging factor." Complicated analysis¹²⁻¹⁵ can calculate the aperture averaged normalized intensity variance, but it is possible to make a simple curve fit to data, and the aperture averaging factors

$$\gamma \approx \frac{0.6}{1 + 100 \sigma_{\mathcal{H}}^4} \quad \text{RESOLVED}, \quad \gamma \approx \frac{12}{1 + 250 \sigma_{\mathcal{H}}^4} \quad \text{UNRESOLVED} \quad (19)$$

appear to give a good simple fit to the data and theory. The Rytov variance or the **nonfluctuating point-source, point-receiver, one-way** propagation "log-amplitude variance" is defined as

$$\sigma_{\mathcal{H}}^2(R) = 0.56 k^{7/6} \int_0^R dz C_n^2(z) (z/R)^{5/6} (R-z)^{5/6} \quad (20)$$

where $C_n^2(z)$ is the refractive index structure coefficient. The path integrals over $C_n^2(z)$ can be numerically integrated for the scenarios of interest.

Similar analysis has been applied to **unresolved** targets in references 16 through 18. Using the larger experimental aperture averaging factor in equation (19), the irradiance pdf of equation (13) can be applied for **unresolved** targets within the atmosphere¹⁸. The Poisson counting distribution in equation (5) must be averaged over equation (13) to include round-trip turbulence effects on photon counting. This has not been analytically evaluated to our knowledge¹⁹, and endo-atmospheric lidar will not be discussed here.

3.0 REVIEW OF TEMPLATE CORRELATION MATCHING

There are many two dimensional image (elevation, azimuth and intensity) correlation filters in the literature²⁰⁻²¹. We summarize them here and how they may be extended to 3D direct-detection lidar images. The correlation process is done in the "spatial-frequency" domain, taking advantage of the fast discrete Fourier transform, denoted FFT. The correlation peaks and their energies (volumes) are independent of the location of the image in the focal plane because the FFT is a linear shift invariant operator. The effects of negative-binomial lidar speckle or shot-noise correlation filtering, either 2D or 3D, have not yet been investigated, to our knowledge.

1) Classical Template Matching (Modified for 3D), Correlation over x,y, & z Simultaneously (TMF)

- 1) Invert a reference image through origin -- x, y, and z location values
- 2) Take 3DFFT
- 3) Store in computer
- 4) Take 3DFFT of each noisy lidar image
- 5) Multiply by reference images for that range
- 6) Take Inverse 3DFFT
- 7) Select max correlation peak or max sum (energy)

2) Template Matching w. Phase-only Filters (PoF)

- 1) Filter = $\exp(j \angle(3\text{DFFT}(\text{reference-image})))$
- 2) Follow steps from 1). Gives sharper correlation peak.

3) Binary Phase-only Filter (BPoF)

- 1) The phase-only filter of 2) is made binary by $H(f_x, f_y) = +1, \cos(\phi) \geq 0; -1$ otherwise
- 2) Follow steps from 1)

4) Symmetric (Normalized) Phase-only Matched Filter (SPoF)

- 1) Filter = $\exp(j \angle(3\text{DFFT}(\text{reference-image}))) / \text{magnitude}(3\text{DFFT}(\text{input-image}))$
- 2) Same steps as 1)

5) Quad-phase-only Filter (QPoF)

- 1) Let $F_{\text{ref}} = 3\text{DFFT}(\text{reference-image})$
- 2) Then, $F_{\text{qpof}} = \text{sgn}(\text{Real}(F_{\text{ref}})) + i \text{sgn}(-\text{Imag}(F_{\text{ref}}))$
- 3) Works better when the reference object has both even and odd components

6) Joint Transform Correlator (JTC)

- 1) **Add** noisy ladar 3D image to reference image (The images may be appended.)
- 2) Take 3DFFT
- 3) Take magnitude squared (PSD)
- 4) Take inverse 3DFFT
- 5) Select correlation peak or max sum (energy)

7) Binary Joint Transform Correlator (BJTC)

- 1) **Add** noisy ladar 3D image to reference image
- 2) Take 3DFFT
- 3) Take magnitude squared
- 4) Select threshold value and $\text{PSD} = 1 > \text{threshold}, = -1 < \text{threshold}$
- 5) Take inverse 3DFFT
- 6) Select correlation peak or max sum (energy)

8) Joint Transform Correlation with Phase-encoded Reference (JTCPR)

- 1) Reference image is multiplied by an inverse 3DFFT{pseudo-random phasors}
- 2) Take 3DFFT of sum
- 3) Take magnitude squared and multiply by pseudo-random phase mask from 1)
- 4) Take inverse 3DFFT
- 5) Select correlation peak or max sum (energy)

9) Inverse Filter (Optimum for Zero Signal-Independent Additive Gaussian Noise, No Speckle)

- 1) Invert reference image through origin -- x, y, and z location values
- 2) Take 3DFFT
- 3) Store in computer
- 4) Take 3DFFT of each noisy ladar image
- 5) Divide by stored filter for that range, element by element
- 6) Take Inverse 3DFFT
- 7) Select max correlation peak or max sum (energy)

10) Inverse Filter, Binarized Input

- 1) The input image and reference image are binarized (0 or 1) by thresholding
- 2) Proceed as in filter 9)

11) Fourier Descriptor Differencing

- 1) The reference images' x and y components are combined to form a complex number, $x + jy$, for each z slice
- 2) A 1D FFT is taken in each z plane
- 3) Translation independence is obtained by ignoring the DC component at the origin for each z
- 4) The magnitude of each Fourier component is taken to eliminate rotation effects
- 5) Size effects are eliminated by dividing the magnitudes by that of element (1) at each z level
- 6) The Fourier descriptors are compared to the same from each ladar measurement via steps 1) to 5), in a least squares difference sense, as the ladar data are taken

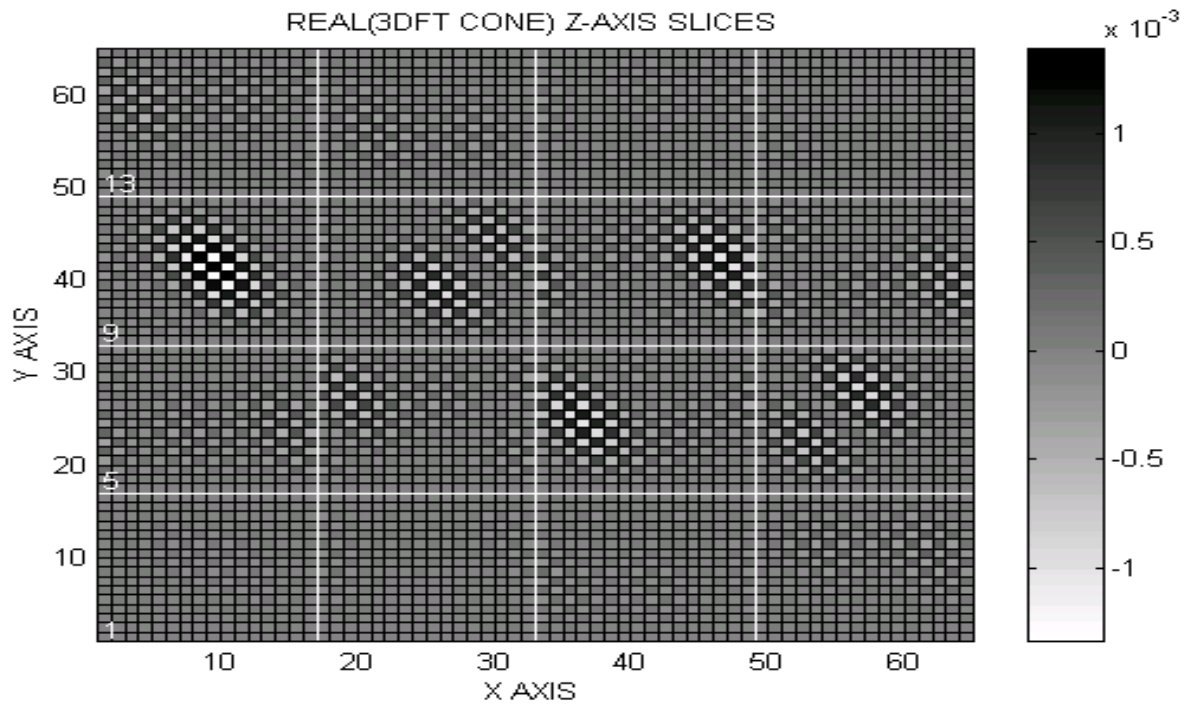


Figure 2. Real part of 3D Fourier transform of 2 m by 1 m cone at 100 km range, 16 z element slices.

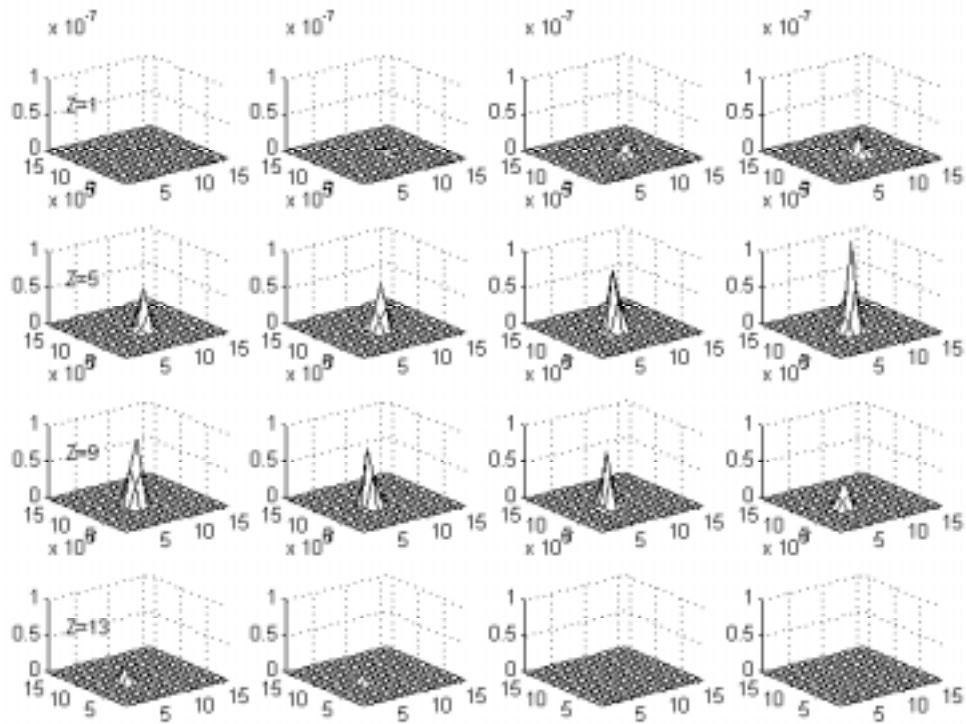


Figure 3. Classical template correlation output in 3D displayed in 16 z-element sections for cone.

A 3D Fourier transform of a 3D cone image to the spatial-frequency domain is difficult to visualize. The real part of a 16x16x16 3DFFT of a 30° azimuth, 0° elevation reference cone image is shown in Figure 2, gray scale coded. The elements are both positive and negative and are displayed in 4x4 z-slices, side by side, as indicated. The imaginary part is roughly 90° out of phase (in 3D) with the real part and is not reproduced here. Following the steps of the classical template matching filter in 1) above, the speckled ladar image is 3DFFTed and multiplied element by element by the stored reference template. The inverse 3DFFT results in a typical correlation output as shown in Figure 3. Figure 3 corresponds to a 2m long, 1m dia. cone at 100 km distance and a total mean photo-electron count per pulse of 400. This is a large signal, typical of the DITP pulse energies and aperture at this range.

3.1 COMBINING REFERENCE IMAGE SETS

Reference image sets of a target at many different aspect angles may be combined to form a more complete reference matrix. Some of these filters from the literature are the “equal correlation peak,” the “minimum average correlation energy,” the “maximum average correlation height,” the “minimum noise and correlation energy,” and the “hybrid composite” filter. The extension of these composite matrix filters to three dimensional images has not yet been examined, to our knowledge.

4.0 TARGET GENERATION

Cone, cylinder, and sphere targets are easily generated by forming x, y, z surface points as a function of the azimuthal angle around the target axis of symmetry, z, and the z-axis height. (The z-axis is also the ladar optical axis.) In this way only 100 or 200 points are needed to describe a target’s surface. Each point is then rotated in azimuth (around x) and then in approximate elevation (around z) by a co-ordinate transform. Each surface point is then assigned a cosine of the angle-of-incidence w.r.t. the laser radar optical axis, z. Using two interpolation routines, the cosines of the angles of incidence and the surface-point z-values are interpolated onto x-y plane elements, 7x7 per detector pixel and in 20 cm range-bins. The cosines of the angle-of-incidence values are then summed (49 points) into each x, y detector pixel range-bin to form a 3D image. Figure 4A shows an example 2 m long, 1 m diameter bi-cone rotated 30° in azimuth and another 30° rotation in (approximate) elevation. Figure 4B shows the 7x7 elements per detector pixel, prior to sorting into the individual pixel range-bins, as determined by the right-side figure in 4B which are the corresponding (over sampled) z values.

In this study each detector pixel is defined to be a square $2.44 \lambda / D_{\text{receiver}}$ or 5.3 μm wide at 532 nm wavelength and a 25 cm aperture. Consequently, in Figure 4C the image is two or three detector pixels across the cone base for a 1 m diameter cone at 100 km range. With this large angular size pixel, convolution with the telescope point-spread function would have a very small effect on the focal plane irradiance distribution as observed by each of these detector pixels. Each detector pixel range-bin output voltage is generated, including target speckle, following equation (12) in Section 2.0. The lower montage in Figure 4C shows a strong-signal, $N_s = 400$ photo-electrons (total) realization which is typical of a 100 km range conical target for the DITP ladar.

5.0 CORRELATION RESULTS TO DATE

The target ranges of interest are from about 50 km to 400 km. The targets of interest are spheres, cones, and cylinders of various sizes. The cones and cone-cylinders may be at aspect angles of from -45° to +45° in elevation and azimuth combinations. This constitutes a very large number of possible ladar

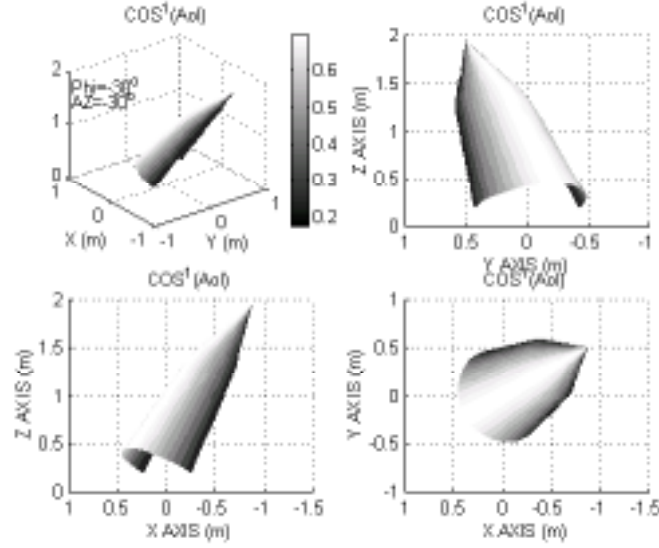


Figure 4A. Bi-cone example at 30° azimuth and 30° elevation. The cosine of the angle of incidence of each element is gray scale coded for projection onto the x-y plane for interpolation at each z level of 20 cm each.

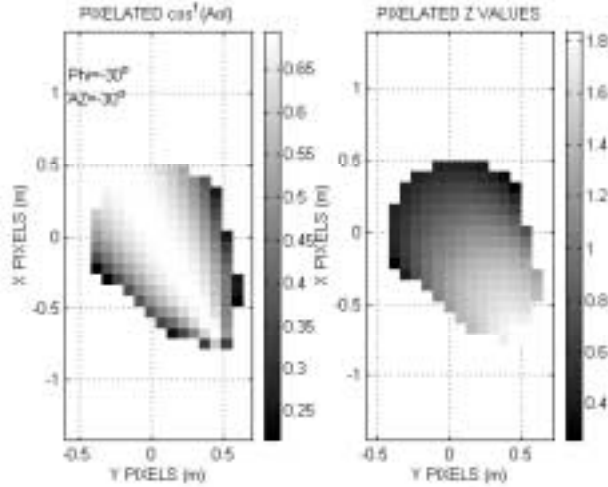


Figure 4B. Interpolated bi-cone cross-section at 7^2 elements per detector pixel at a target range of 100 km. Corresponding z-axis values (gray scaled) are indicated on the right side for partitioning into the range-bins.

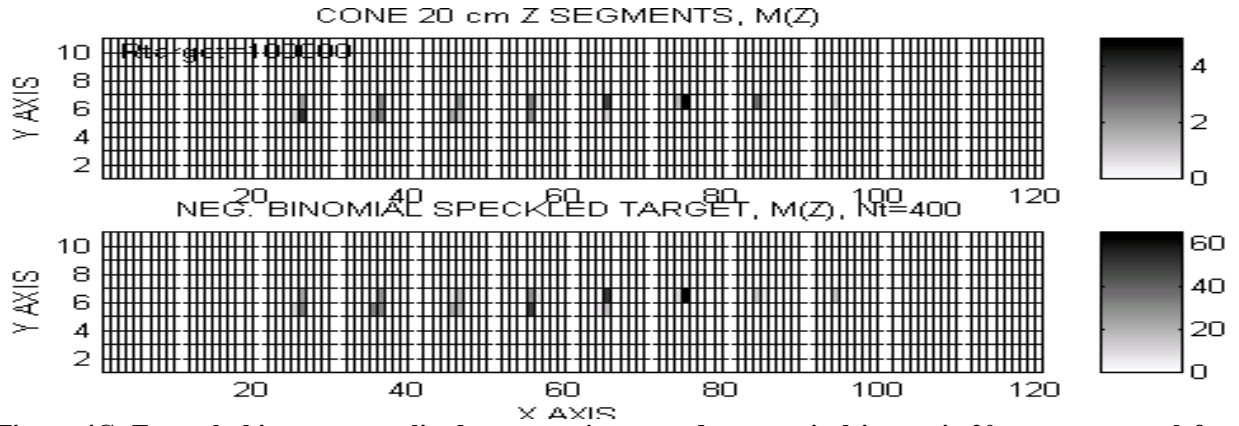


Figure 4C. Example bi-cone normalized cross-sections per detector pixel in z-axis 20 cm segments, left to right. Lower montage is one speckle realization in millivolts, following equation (12) applied to each pixel range-bin.

measurements. We point out here that, having acquired an object, the ladar very accurately determines the range to the object via time-of-flight. Thus, we would know exactly which reference template range-set to use, thereby greatly reducing the number of reference templates. At this point in our research we have examined the performance of filters 1) Classical Template Matching Filter (CTMF), 2) Phase-only Filter (PoF), 3) Binary Phase-only Filter (BPoF), 4) Symmetric Phase-only Filter (SPoF), 6) Joint Transform Correlator (JTC), and 9) Inverse Filter. Since we normalize the 3DFT of the reference image and the 3DFT of the ladar signal image as it comes in to compare correlation voltage outputs, the PoF below is really the SPoF.

5.1 INVERSE FILTER STUDIES

The inverse filter (number (9)) is the optimum filter for no signal-independent additive noise and no target surface speckle (signal-dependent noise). A thumb-tack or delta function correlation peak results when the correct template is selected. However, when ladar speckle and shot-noise effects are included, the small magnitude spatial-frequency domain components of the reference template are no longer divided into the same small magnitude elements from the ladar data (speckled) image. The inverse-filter therefore blows up to large unrealistic values at certain locations in the correlation output. At this point in the 3D filter study, we eliminate the inverse-filter from consideration. It may be possible to apodize or constrain this filter, or it may be possible to combine the inverse-filter with other filters for more robust correlation outputs. This concept will be investigated in the future.

5.2 SIGNAL STRENGTH VS SPECKLE MONTE CARLO STUDIES

We first examine the effects of negative-binomial speckle and shot-noise on the 3D correlators assuming we have selected the correct reference image template. We take a 2 m long, 1 m diameter cone at 100 km range and 30° aspect angle in azimuth and examine the fluctuation of the correlation peaks relative to the mean peak value for decreasing total photo-electron counts. We also look at the “width” of the 3D correlation peak by finding the second largest correlation value which is in an adjacent z-axis range-bin for this target. If this value were 0.5, then the full-width at half maximum would be approximately two z elements. In Table I are the results of 51 Monte Carlo runs for each level of mean

Table I. Correlation Peak Fluctuations and Second (adjacent) Maximum Magnitude (\approx Width) vs N_s

Range	N_s	Az.	El.	CTMF		PoF		BpoF		JTC*	
				$\sigma/\langle v \rangle$	Width	$\sigma/\langle v \rangle$	Width	$\sigma/\langle v \rangle$	Width	$\sigma/\langle v \rangle^*$	Width*
100k	400	30°	0°	.080	.74	.098	.58	.106	.69	.033	.66
	200			.083	.76	.121	.60	.122	.70	.038	.64
	100			.070	.77	.109	.61	.124	.73	.034	.65
	50			.093	.75	.130	.57	.114	.68	.040	.64
	25			.091	.75	.131	.56	.138	.67	.034	.63
	12			.101	.78	.124	.58	.120	.71	.035	.60
	6			.139	.75	.150	.56	.151	.74	.028	.55
	3			.285	.78	.237	.67	.221	.79	.022	.49
	3			.193	.74	.223	.61	.193	.80	.052	.50
200k	50	30°	30°	.078	.74	.096	.55	.093	.66	.047	.65
	12			.087	.71	.094	.49	.102	.70	.050	.61
	3			.193	.74	.223	.61	.193	.80	.052	.50

* Includes peak from reference image.

total photo-electrons, N_s , for filters number 1), 2), 3), and 6). Each 3D detector image output is corrupted by 250 μ V rms of additive Gaussian baseline noise and thresholded at 750 μ V following the data fits of Section 2.3 and Figure 1A. The first row, where $N_s = 400$, corresponds to Figure 3 above. We see that

speckle and shot-noise do not seriously further degrade the peak fluctuations until the mean total count (N_s) is less than 12 photo-electrons or about **1 p.e. per pixel-range-bin**. The normalized standard deviation of the Joint-Transform-Correlator (JTC) is the smallest, due to the addition of the reference and measured images, followed by the Classical Template Matched Filter (CTMF), the Phase-only-Filter (PoF), and Binary-Phase-only-Filter (BPoF). The correlation-peak 3D-width of the **PoF is the narrowest**, followed by the JTC, BPoF, and CTMF. We note that a correlation filter output “peak to mean ratio,” an often used statistic, is not relevant here due to these target speckle fluctuations.

5.3 LARGE SIGNAL, TARGET ASPECT ANGLE SPECKLE STUDY

Next, we take the nominal 2 m long by 1 m diameter cone target and a typical strong-signal return of $N_s = 400$ photo-electrons at 100- km range and examine the variation in correlation peak and peak width as a function of aspect angle. At this nominal strong signal level, all output fluctuations are caused by speckle and shot-noise. In Table II we see that the PoF again produces the narrowest 3D peak width

Table II. Peak Fluctuations and Second (adjacent) Maximum Magnitude (\approx Width) vs Aspect Angle

Range	N_s	Az.	El.	CTMF		PoF		BPoF		JTC*	
				$\sigma/\langle v \rangle$	Width	$\sigma/\langle v \rangle$	Width	$\sigma/\langle v \rangle$	Width	$\sigma/\langle v \rangle^*$	Width*
100k	400	30°	0°	.080	.74	.098	.58	.106	.69	.033	.66
		30°	15°	.083	.74	.096	.55	.111	.73	.038	.66
		30°	30°	.093	.77	.100	.56	.113	.74	.044	.68
		15°	0°	.083	.87	.132	.69	.131	.78	.060	.80
		15°	15°	.080	.85	.143	.64	.142	.76	.082	.77
		15°	30°	.082	.84	.129	.63	.129	.72	.072	.76

* Includes correlation peak from reference image.

followed by the BPoF, JTC, and CTMF widths respectively. The JTC has a somewhat smaller normalized peak standard deviation than the CTMF, which is smaller than those of the PoF and BPoF correlators. We also see that the JTC, PoF, and BPoF peak standard deviation increases when the cone is at 15° aspect angle, presumably due to the reduced x and y image extent.

5.4 JOINT TRANSFORM CORRELATOR REFERENCE-IMAGE PEAK

The JTC filter creates a correlation peak due to the reference image. This is added to the correlation peak from the image data. Consequently, the JTC normalized standard deviations and widths found in Tables I and II are misleading -- the variation due to speckle relative to the image data peak is much larger. We have attempted to remove the reference image correlation peak following 2D approaches²³⁻²⁴ but found them not to work in 3D application using the spatial-frequency domain calculations. We are currently investigating the removal of this reference image produced correlation peak. Otherwise, we note that from Tables I and II the **CTMF has the least sensitivity to ladar speckle** and that the **PoF has the narrowest correlation peak**.

5.5 IMAGE DISPLACEMENT EFFECTS

The Fourier transform is a linear shift invariant operator. The correlation peaks and their energies (the volume sum) should remain constant as the data image moves in x, y, and z across the detector focal plane and the range-bins. This is shown to be true for **integer** pixel translations of multiples of 0.2 m in z and/or $5.2\mu\text{r} \times \text{target range} = 0.52 \text{ m}$ in x or y for this study. However, as the image translates **between** integer pixel centers, the correlation peak spreads to the adjacent 4 or 6 nearest neighbors. This is shown in Table III:

Table III. Image Displacement Effects on Correlation Peaks.

R	N _s	Az.	El.	$\Delta x, \Delta y, \Delta z$	CMTF		PoF		JTC*	
					Peak (loc.)	E	Peak (loc.)	E	Peak (loc.)*	E*
100k	320	30°	30°	0, 0, 0 (m)	1.000 (8,8,8)	1.43	1.000 (8,8,8)	1.92	1.000 (9,9,9)	5.73
				0, .52, 0	0.995 (8,9,8)	1.44	0.992 (8,9,8)	2.05	0.991 (9,9,9)	5.76
				-.52, 0, 0	0.989 (7,8,8)	1.41	0.996 (7,8,8)	1.90	0.986 (9,9,9)	5.75
				-.52, .52, 0	0.991 (7,9,8)	1.42	0.996 (7,9,8)	1.96	0.869 (9,9,9)	5.70
				0, 0, .2	0.999 (8,8,9)	1.43	1.000 (8,8,9)	1.92	1.130 (9,9,9)	5.73
				0, 0, .1	0.903 (8,8,8)	1.47	0.803 (8,8,8)	2.37	1.056 (9,9,9)	5.87
					0.919 (8,8,9)		0.783 (8,8,9)			
				0, .26, 0	0.741 (8,8,8)	1.51	0.631 (8,9,8)	3.28	1.023 (9,9,9)	6.04
					0.725 (8,8,7)		0.549 (8,8,7)			
					0.666 (8,9,9)					
				-.26, 0, 0	0.787 (7,8,9)	1.40	0.631 (7,8,9)	2.94	0.972 (9,9,9)	5.58
					0.713 (8,8,7)		0.545 (8,8,8)			
				-.26, .26, 0	0.611 (8,8,6)	1.30	0.496 (8,8,6)	3.37	0.926 (9,9,9)	5.21
					0.570 (8,8,7)		0.557 (7,9,9)			
					0.638 (8,9,9)					
				-.26, .26, .1	0.725 (8,8,7)	1.50	0.545 (8,8,7)	3.62	1.009 (9,9,9)	6.02
					0.723 (7,8,10)		0.545 (7,9,10)			

* Includes correlation peak from reference image.

Table III considers the 2m long, 1m diameter cone rotated 30° in azimuth and 30° in elevation. The reference image is perfectly centered in the focal plane and the data image is translated as indicated. We see that the energies of the CMTF and JTC are relatively insensitive to data image translations w.r.t. the fixed reference image. The peak of the JTC is again insensitive to data image movement (including the reference image peak), and that the CMTF has about a 30% variation throughout one x, y, z pixel translation. The PoF has about a 50% variation in correlation peak value throughout one pixel translation, and the filter energy also varies by about 50%.

5.6 CORRELATION OF CONE VS SPHERES STUDY

We next use the cone at 30° elevation and 30° azimuth as the reference image and spatial-frequency domain template and correlate this with spheres of radii of 0.75, 1, and 2 m translated across a pixel. The results shown in Table IV can be compared to those of Table III, and we see that the correlation peaks are about 1/2 to 1/3 of the cone-cone correlation peaks. The filter energies are also comparable due to a broadening of the correlation peaks. Since these reduced peaks are about 6 σ to 7 σ below the speckle fluctuation of the correct cone-cone peak, good discrimination of cones from spheres

Table IV. Correlation Peaks and Energies of Spheres vs Cone at 30° Az and 30° Elevation.

				CMTF		PoF		JTC*	
R	N _s	Sphere Dia. & Δx, Δy, Δz		Peak (loc.)	E	Peak (loc.)	E	Peak (loc.)*	E*
100k	320	1 m	0, 0, 0 (m)	0.594 (8,8,8)	1.20	0.492 (8,8,8)	4.40	0.981 (9,9,9)	4.84
		2 m	0, 0, 0	0.375 (8,8,11)	1.51	0.434 (8,8,11)	4.71	1.111 (9,9,9)	6.05
		0.75 m	0, 0, 0	0.530 (8,8,9)	1.38	0.451 (8,8,9)	4.32	1.065 (9,9,9)	5.53
		1 m	0, .52, 0	0.369 (8,9,10)	1.49	0.451 (8,9,10)	4.61	0.972 (9,9,9)	5.97
		1 m	0, .26, 0	0.375 (8,8,8)	1.57	0.455 (8,9,11)	4.47	1.051 (9,9,9)	6.30
		1 m	-.26, .26, 0	0.389 (8,8,8)	1.64	0.455 (7,9,11)	4.38	0.955 (9,9,9)	6.57
		1 m	-.26, .26, .1	0.372 (7,9,9)	.601	0.525 (7,9,9)	3.40	0.801 (9,9,9)	2.88
		1 m	-.26, .26, .2	0.407 (8,8,7)	.614	0.455 (8,8,7)	3.46	0.796 (9,9,9)	2.93

* Includes correlation peak from reference image.

can be made. This capability should apply out to 200 km since $N_s \approx 40$ at 200 km which is > 1 pe per voxel. Also, we see that the JTC again adds the correlation peak from the sphere, thus the sphere-cone JTC peaks are unacceptably large under the present filter implementation.

5.7 CONE ASPECT ANGLE SENSITIVITY

We again use the 2m long, 1m diameter cone at 30° elevation, 30° azimuth and 100 km range as the reference image with its spatial-frequency domain template and correlate this with identical cones at various aspect angles. In Table V we see that going from an aspect angle of 30° to 15° causes a $>20\%$ reduction in correlation peak size. Changes in the elevation angle at the same aspect angle result in only

Table V. Cone Image Rotation Effects on Correlation Peak w.r.t. Cone at 30° Az, 30° El.

R	N_s	Image		CMTF		PoF		JTC*	
		Az.	El.	Peak (loc.)	E	Peak (loc.)	E	Peak (loc.)*	E*
100k	320	30°	30°	1.000 (8,8,8)	1.43	1.000 (8,8,8)	1.92	1.000 (9,9,9)	6.11
		30°	15°	0.998 (8,8,8)	1.53	0.914 (8,8,8)	2.69	1.042 (9,9,9)	6.68
		30°	0°	0.961 (8,8,8)	1.66	0.824 (8,8,8)	3.95	1.106 (9,9,9)	6.12
		30°	-15°	0.726 (8,8,8)	1.53	0.570 (8,8,8)	4.75	1.056 (9,9,9)	5.70
		30°	-30°	0.590 (8,8,8)	1.43	0.520 (8,8,8)	4.89	1.046 (9,9,9)	5.73
		15°	30°	0.745 (8,8,8)	1.65	0.590 (8,8,8)	3.92	1.014 (9,9,9)	6.62
		15°	15°	0.779 (8,8,8)	1.71	0.615 (8,8,8)	4.08	1.306 (9,9,9)	6.90
		15°	0°	0.840 (8,8,8)	1.81	0.664 (8,8,8)	4.55	1.370 (9,9,9)	7.35
		15°	-15°	0.764 (8,8,8)	1.71	0.643 (8,8,8)	4.70	1.306 (9,9,9)	6.90
		15°	-30°	0.671 (8,8,8)	1.65	0.135 (8,8,8)	4.90	1.292 (9,9,9)	6.62

* Includes correlation peak from reference image.

a few percent decrease in the correlation peak at this 30° reference image angle. When the aspect (azimuth) angle is decreased to 15° , a 25% - 40% decrease in filter peak is observed. Since this is 3σ to 5σ below the correct cone-cone peak, reasonably robust discrimination of a difference of 15° in aspect is possible out to ≥ 200 km. Due to the spread in the correlation peaks and the increase in side peaks, the energies of the three filters increases.

5.8 RANGE-BIN OUTPUT CONCATINATION WITH 2D FILTERING

In Figure 4C above we see that it is possible to arrange the detector outputs, 10×10 pixels in this study, into a “montage plot” where the range-bin outputs are placed side by side, from left to right. This obviously constitutes a **2D matrix** which can be processed following the 2D template matching filters from the literature without modification. For a maximum target length of 2 m, the image matrix would become 10×110 elements or less depending on aspect angle. We note that all measurement information is contained within this 2D matrix, and the ladar data image will always be within ± 0.5 range-bin pixels of the reference image. This may then be zero padded to $16 \times 128 = 2048$ elements vs the $16 \times 16 \times 16 = 4096$ elements for 3D processing. One template correlation would therefore require about 300 k FLOPs which is less than one half of the 650 k FLOPs required for a single 3D correlation. Consequently, we have terminated 3D Monte Carlo studies temporarily to investigate this concept and its sensitivity to negative-binomial speckle driven shot-noise.

6.0 SUMMARY AND CURRENT WORK

In this initial study we are introducing the concept of three-dimensional spatial-frequency domain correlation filtering for target recognition and identification. This follows an extrapolation of current two-dimensional filter algorithms. The use of the spatial-frequency domain is important because the correlation peaks and energies are independent of the image location in the focal plane for integer x, y, and z voxel displacements. The correct ladar speckle and shot-noise effects are complicated and detector dependent, and these are summarized in Section 2.0. The effects of round-trip turbulence on endo-atmospheric ladar operation are also complicated and have not yet been fully solved, as also discussed in Section 2.0.

This exo-atmospheric study with partially resolved cones and spheres and with no clutter or dark counts but with Gaussian base-line noise has shown that the 3D Phase-only-Filter (PoF) produces the narrowest 3D correlation peaks of the filters studied. Small fluctuations of 8% to 10% in the correlation filter peaks for all the filters due to speckle have been demonstrated. Robust separation of spheres from cones has been demonstrated out to >200 km. Cone vs cone aspect angle determination is not nearly as robust, due to the geometries involved, and needs to be further investigated. The 3D JTC and 3D Inverse filters need to be modified to be useful. About 1 mean photo-electron per voxel produces strong correlation peaks. We are now implementing target range-slicing and 2D image formation by concatenation to implement 2D correlation filters as discussed in Section 5.8. We also note that 3D template correlations may supplement or refine less computationally intensive algorithms such as total signal, range-extent, x-z, y-z, and x-y plane image centroid estimation, and image moments.

7.0 ACKNOWLEDGEMENTS

This work was partially sponsored under BMDO/NRL contract N00014-97-D-2014 supporting the Discriminating Interceptor Technology Program. The authors would like to thank Dr. Frank Hanson, executing agent; LCDR James Buckley, program manager; and Dr. Walter Dyer, technical advisor, for their support and guidance. The authors would also like to thank Tom Driscoll and Paul Titterton of EOO, Inc., Guy Beaghtler of Fibertek, Inc., and Verle Aebi of Intevac, Inc. for useful technical discussions concerning the DITP ladar system and breadboard ladar and target experimental test results.

8.0 REFERENCES

1. Goodman, J., "Some Effects of Target-Induced Scintillation on Optical Radar Performance," Proc. IEEE, Vol. 53, No. 11, Nov. 1965.
2. Goodman, J., "Comparative Performance of Optical-Radar Detection Techniques," IEEE Trans. AES, Vol. AES-2, No. 5, Sept. 1966.
3. Goodman, J., *Laser Speckle and Related Phenomena*, J.C. Dainty Ed., Springer-Verlag, 1975, Second Edition, 1984.
4. Saleh, B., *Photoelectron Statistics*, Springer-Verlag, 1978.
5. Youmans, D., Hart, G., "Numerical evaluation of the "M" parameter for direct detection ladar," SPIE Proc. Vol. 3380, April 1998.
6. Teich, M., B. Saleh, "Effects of random deletion and additive noise on bunched and anti-bunched photon counting statistics," Opt. Lett, Vol. 7, No. 9, Aug. 1982.
7. Papoulis, *Probability, Random Variables, and Stochastic Processes*, McGraw-Hill, 1965, p. 127.
8. Papoulis, p. 37.
9. Papoulis, p. 193.
10. Papoulis, p. 560.

11. Pratt, W. K., *Laser Communication Systems*, John Wiley, 1969, p.260.
12. Lee, M., F. Holmes, R. Kerr, "Statistics of speckle propagation through the turbulent atmosphere," J. Opt. Soc. Am. 66, Nov. 1976.
13. Holmes, F., M. Lee, R. Kerr, "Effect of the log-amplitude covariance function on the statistics of speckle propagation through the turbulent atmosphere," J. Opt. Soc. Am. 70, April 1980.
14. Gudimetla, R., F. Holmes, R. Elliott, "Two-point joint-density function of the intensity for a laser-generated speckle field after propagation through the turbulent atmosphere," J. Opt. Soc. Am. A 7, June 1990.
15. Gudimetla, R., Holmes, J. Opt. Soc. Am. 72, Sept. 1982.
16. McIntyre, C., Kerr, Lee, Churnside, "Enhanced variance of irradiance from target glint," Appl. Opt. 18, 1 Oct. 1979.
17. McIntyre, C., Lee, Churnside, "Statistics of irradiance scattered from a diffuse target containing multiple glints," J. Opt. Soc. Am. 70, Sept. 1980.
18. Youmans, D., R. Gudimetla, "Round-trip turbulence scintillation effects on laser radar: Monte Carlo simulation results for unresolved targets," SPIE Proc. Vol. 3065, *Laser Radar Technology and Applications II*, April 1997.
19. Diamant, P., M. Teich, "Multiply stochastic representations for K distributions and their Poisson transforms," J. Opt. Soc. Am. A, Vol. 6, Jan. 1989.
20. Duda, R., Hart, P., *Pattern Classification and Scene Analysis*, John Wiley and Sons, 1973, Chapter 8.
21. Gonzalez, R., Woods, R., *Digital Image Processing*, Addison-Wesley, 1992, Chapter 9.
22. Driscoll, T., et al., "Comparison of Theory and Experiments in the Effects of Speckle on NMD/TMD Target Recognition with Direct-Detection LADAR," Proc. IRIS Active Systems, Feb. 1999.
23. Takanori, N., "Phase-encoded joint transform correlator to reduce the influence of extraneous signals," Appl. Opt., Vol. 37, No. 17, 10 June 1998.
24. Li, C., et al., "Nonzero-order joint transform correlator," Opt. Eng., Vol. 37, No. 1, Jan. 1998.